A subsurface Indian Ocean dipole response to tropical volcanic eruptions

Takeshi Izumo, Myriam Khodri, Matthieu Lengaigne, Iyyappan Suresh

A subsurface Indian Ocean Dipole response to tropical volcanic eruptions

Takeshi Izumo[1,2], Myriam Khodri[1], Matthieu Lengaigne[1,2], Iyyappan Suresh[3]

[1]*IRD, LOCEAN-IPSL, Sorbonne Univ. (UPMC, Univ Paris 06)-CNRS-IRD-MNHN, Paris, France*

[2]*Indo-French Cell for Water Sciences, IISc-NIO-IITM-IRD Joint International Laboratory, NIO, Goa, India*

[3]*CSIR-National Institute of Oceanography, Goa, India*

Corresponding author:

T. Izumo, takeshi.izumo@ird.fr

Key Points:

- Tropical volcanic eruptions induce a subsurface ocean response typical of a negative Indian Ocean Dipole (IOD).

- The subsurface response results from equatorial westerlies driven by the large land cooling over Africa.

- The surface signature differs from that of an IOD, with a cooling larger in the northwest than southeast Indian Ocean as a result of the climatological cloud cover distribution.

29   **Abstract.** The impacts of explosive volcanism on the densely-populated Indian

30   Ocean (IO) region remain elusive. Dedicated sensitivity experiments indicate that

31   tropical volcanic eruptions induce a stronger surface cooling over Africa than of ocean,

32   promoting westerlies in the equatorial IO. These westerlies drive a subsurface response

33   reminiscent to that of a negative IO Dipole (IOD) during autumn in the year of eruption.

34   The eruption also drives an enhanced cooling over the northwestern IO as a direct

35   response to climatological cloud cover distribution. The resulting anomalous zonal sea

36   surface temperature gradient contributes to enhance equatorial westerly anomalies in

37   summer. The response is sensitive to the IO preconditioning, being larger when the

38   system is favourable to a positive IOD development. Volcanic eruptions also induce a

39   subsurface IOD-like response in the multi-model database from the Coupled Model

40   Intercomparison Project Phase 5 as well as a primary productivity decrease in the

41   eastern IO.

42

43   **Plain text summary.** Explosive volcanism induces a global surface cooling but its

44   regional impact on the densely-populated Indian Ocean sector is poorly documented.

45   Here we show that the volcanic eruptions induce a subsurface ocean response in

46   autumn of the eruption's year, reminiscent to that of a negative Indian Ocean Dipole, an

47   intrinsic climate mode in the Indian Ocean equivalent to El Niño in the Pacific. This

48   subsurface response is driven by equatorial westerly anomalies resulting from the

49   stronger surface cooling over the African landmass than over the ocean. The response is

50   sensitive to the Indian Ocean preconditioning, being larger when the system is

51   preconditioned towards a positive Indian Ocean Dipole development.

52

1) Introduction

The densely populated region surrounding the Indian Ocean (IO) is socio-economically very sensitive to climate variability. As Sea Surface Temperatures (SSTs) in the IO often exceeds the 28°C threshold for deep atmospheric convection (e.g. Graham and Barnett, 1987), small SST perturbations can force a significant atmospheric response. This sensitivity promotes active air-sea interactions, which give rise to the Indian Ocean Dipole (IOD; Reverdin et al. 1986, Saji et al. 1999, Webster et al. 1999, Murtugudde et al. 2000), an intrinsic mode of climate variability in the IO equivalent of El Niño/La Niña Southern Oscillation (ENSO) in the Pacific. A negative IOD (nIOD) is characterized by a surface warming and an anomalously deep thermocline off the west coasts of Java and Sumatra and by a cooling and anomalously shallow thermocline anomalies in the west IO, driven by anomalous westerlies over the central equatorial IO. A positive IOD (pIOD) is characterized by opposite anomalies. IOD events usually develop in boreal summer and peak in autumn. El Niño and La Niña events respectively favour positive and negative IODs, but IOD can also occur independently of ENSO (e.g. Annamalai et al. 2003; Yamagata et al. 2004). The IOD has important implications at regional scale on the IO climate and monsoon (e.g. Schott et al. 2009), tropical cyclones (Xie et al. 2002), oceanic primary production (Curie et al. 2013) and oxygen (Vallivattathillam et al. 2017), and also at global scale by influencing the Madden-Julian Oscillation (e.g. Izumo et al. 2010b) and ENSO (e.g. Izumo et al. 2010a, 2014, 2016, Jourdain et al. 2016).

Stratospheric tropical volcanic eruptions induce a temporary global radiative cooling that directly impacts the earth climate by inducing a surface cooling at the global scale (see Robock, 2000 for a review). This cooling is larger on land than on ocean, resulting in an overall rainfall reduction over the tropical landmass (e.g. Schneider et al. 2009, Joseph and Zeng 2011, Iles and Hegerl 2014). The upper ocean cooling translates into an Oceanic Heat Content (OHC) decrease (e.g. Church et al. 2005, Gleckler et al. 2006, Stenchikov et al. 2009, Mignot et al. 2011). The climatological cloud cover and oceanic mixed layer depth (MLD) distributions however induce a spatially inhomogeneous ocean cooling: e.g. a clear sky and thin MLD induces a larger cooling (McGregor and Timmerman 2011, Ohba et al. 2013). Such land/sea thermal contrast and inhomogeneous ocean cooling also results in specific regional climate

86   responses. Notably, Khodri et al. (2017, hereafter K17) demonstrated using dedicated
87   sensitivity experiments that the larger cooling over tropical Africa than over the ocean
88   force westerlies over the western Pacific, hence favouring an El Niño the year following
89   the eruption.

90   While the Pacific response to tropical volcanic eruptions has been extensively
91   documented (see K17 and the references therein), there is to date no study focusing on
92   the detailed response of the IO to these eruptions. The present study aims to fill this gap
93   by analysing the Pinatubo-forced sensitivity experiments designed in K17 as well as
94   simulations from the Coupled Model Intercomparison Project phase 5 (CMIP5; Taylor et
95   al. 2012).

96

97   ## 2) Models, experimental strategy and methods

98   ### 2.1 The IPSL-CM5B LR model and the experimental strategy

99   In this study, we use the same set of simulations as in K17 performed with the IPSL-
100   CM5B-LR climate model (cf. Supplementary Information – hereafter SI, its section 2, for
101   details on the modelling setup). This model couples the LMDZ5B (Hourdin et al. 2013)
102   atmospheric and NEMO3.2 (Madec 2015) oceanic components, and accurately captures
103   the main observed IOD characteristics (Jourdain et al. 2016).

104   We focus on the Pinatubo eruption (June 15th, 1991), as it is the strongest and best-
105   observed tropical stratospheric eruption during the instrumental period. The main set
106   of coupled (CPL hereafter) simulations consists of a pair of 3-year-long ensemble
107   experiments of 30 members each with (PTUBO) and without (CTL) a Pinatubo-like
108   forcing. These simulations are initialized on June 1st of a selected year from the historical
109   simulation (with neutral El Nino Southern Oscillation (ENSO) conditions in the absence
110   of volcanic forcing, avoiding any interference with external ENSO forcing).

111   The CPL response to volcanic forcing is assessed by performing the difference
112   between PTUBO and CTL experiments (CPL = PTUBO-CTL), internal climate variability
113   being reduced by the ensemble average. Significance and confidence intervals are
114   computed from usual two-tailed Student t-tests, each member being an independent
115   degree of freedom.

116   We also analyse the following dedicated atmospheric experiments performed with
117   the atmospheric component of the IPSL-CM5B model (K17). They are forced by the

118   coupled model outputs to assess the dominant mechanisms driving the IO response:

119   (1) ATM experiments assess the direct effect of volcanic radiative forcing on clouds
120   and atmospheric vapour content (Soden et al. 2002).

121   (2) OCEAN experiments assess the indirect effects of volcanic forcing on the
122   atmospheric response through the SST inhomogeneous cooling.

123   (3) LAND experiments quantify the effect of the stronger cooling over land than
124   over the ocean. An additional sensitivity experiment finally isolates the specific role of
125   the cooling over African landmass (LAND-Africa).

126   Finally, the relevance of the two-tier approach is assessed using an experiment
127   including all these three processes (ALL).

2.2 Linear Continuously Stratified (LCS) and slab ocean models

129   The equatorial IO dynamical response to windstress anomalies resulting from each
130   sensitivity experiment is then estimated by forcing a Linear Continuously Stratified
131   (LCS; McCreary, 1980) ocean model of the Indo-Pacific region (Izumo et al. 2016, 2018
132   configuration; cf. SI). This LCS realistically simulates sea surface height (SSH) variations
133   in the Indo-Pacific region (Suresh et al. 2013, 2016; Izumo et al. 2016, 2018), despite
134   being linear and simple.

135   A simple slab ocean mixed layer equation using a spatially-varying monthly
136   climatological mixed layer depth is also used, to simulate the SST thermodynamical
137   response to the eruption-induced Short-Wave (SW) flux anomalies (see SI), following
138   the approach of McGregor and Timmerman (2011).

2.3 CMIP5 simulations

The robustness of the response from our single model experiments is further

assessed by analysing historical simulations from the CMIP5 multi-model dataset over

the 1861-2005 period (Suppl. Table S1). As reported in many previous studies (e.g.

Jourdain et al. 2016), CMIP5 simulations, in general, accurately capture the IOD

seasonality and pattern but overestimate its amplitude. Their response to tropical

volcanism is estimated here by compositing the 5 largest historical tropical eruptions,

keeping in mind that these eruptions exhibit different amplitudes and seasonal

evolutions (cf. Fig. S1).

We use the classical Dipole Mode Index (DMI, the SST difference between 50-70°E,

10°N-10°S west and 90-110°E, 0-10°S east poles; Saji et al. 1999) to identify IOD events,

as well as the SSH averaged over the DMI eastern pole box, the SSH being an accurate

proxy for OHC and thermocline depth variations (Rebert et al. 1985).

3) Results

Figure 1ac displays the surface and ocean subsurface ensemble mean CPL response

to the Pinatubo eruption. As expected, there is an overall cooling over the IO region,

stronger over land than at the ocean surface. The SST cooling is larger over the

northwest than over the southeast IO, leading to a northwest-southeast anomalous SST

gradient (Fig. 1a), which translates into a dipolar pattern in terms of relative SST (i.e.

SST minus its 20°N-20°S tropical mean; cf. SI, K17; Held and Soden 2006; Vecchi and

Soden 2007) and precipitation (Fig. S2). The equatorial IO is also characterized by

significant westerly/north-westerly anomalies, larger in the eastern IO. The SSH and

related subsurface oceanic response (Fig. 1c) is typical of a negative IOD (cf. Fig. S3;

Murtugudde et al. 2000, Currie et al. 2013), with a downwelling signal along the coast of

Java and Sumatra and the Bay of Bengal rim and an upwelling signal in the central and

western IO maximum off the equator.

The LCS experiment forced by CPL ensemble wind stress (Fig. 1d) accurately

captures the major SSH signature simulated by the coupled model (Fig. 1c),

demonstrating that linear ocean dynamics explains most of the coupled model response.

There is however a positive SSH offset over the entire IO, because the LCS physics

cannot simulate in essence the SSH decrease related to the overall upper ocean cooling

172   driven by volcanically-induced surface heat flux anomalies (e.g. Church et al. 2005,
173   Gleckler et al. 2006, Stenchikov et al. 2009). The volcanically-induced wind stress
174   anomalies easily explain the SSH dipolar pattern: equatorial westerlies indeed induce
175   downwelling equatorial Kelvin waves deepening the thermocline in the eastern IO and
176   westward propagating equatorial Rossby waves shallowing the thermocline in the
177   central and western IO.

178   As the IO subsurface response to volcanic forcing is qualitatively similar to that of a
179   negative IOD (hereafter nIOD) but different at the surface, we will term this response as
180   a « volcanic subsurface nIOD ». This ensemble mean response is about one-third to a half
181   of the typical SSH amplitudes during a typical IOD simulated by the IPSL model (Fig. S3).
182   It is significant at the 99% level for the DMI east pole SSH. The SST pattern is different
183   from that of a typical IOD (Fig. S3), although it projects onto DMI poles (Figs 1a and S2a),
184   leading to a significant negative DMI anomaly of -0.4°C.

185   The subsurface ocean response is largely wind driven (Fig. 1cd). We hence analyse
186   the dedicated sensitivity atmospheric experiments described in Section 2 to understand
187   the mechanisms responsible for the anomalous equatorial westerlies. The similar wind
188   patterns depicted in CPL and ALL experiments confirm the relevance of this two-tier
189   approach (Fig. 1ab). Despite a 30% overestimation of the CPL response at its peak, the
190   temporal evolution of equatorial zonal wind-stress (Fig. 2a) and SSH (Fig. 2c) anomalies
191   in ALL experiment are also not statistically distinguishable as a result of the large inter-
192   members spread. LAND process explains most of the equatorial westerly anomalies and
193   related east IO downwelling (Fig. 2b,d). OCEAN process also modestly contributes to
194   these westerly and eastern IO downwelling anomalies at the end of the summer. Finally,
195   ATM influence is negligible, and will not be further discussed. Figure 2e shows the
196   corresponding surface temperature and wind-stress patterns in autumn for the LAND
197   experiment. As expected from Figure 2b, LAND experiment exhibits equatorial
198   westerlies similar to those in ALL and PTUBO CPL experiments in the equatorial region
199   (Fig. 1). LAND also displays additional strong northeasterly winds in the Arabian Sea,
200   consistent with the expected thermal wind response to the Arabic peninsula cooling (e.g.
201   Samson et al. 2016).

202   Applying the LAND cooling only over tropical Africa (LAND-Africa) results in a
203   similar equatorial zonal wind (Fig. 2b,f) and SSH (Fig. 2d) evolution as those depicted for
204   LAND, implying that these equatorial westerlies are mainly driven by the African land

205 cooling (K17). These westerly anomalies are however shifted northward in this LAND-
206 Africa experiment, most likely because of the absence of the Asian land cooling and
207 related winter monsoon-like circulation anomalies in the eastern Arabian Sea and Bay of
208 Bengal. The African cooling reduces the rainfall and related diabatic heating locally,
209 thereby inducing a Matsuno-Gill response (Gill 1980) with an equatorial atmospheric
210 Kelvin wave forcing to the east of the heating anomaly, consistent with K17 finding.
211 Milder - but significant - westerly anomalies developing in the central east equatorial IO
212 in July-August in OCEAN experiment (Fig. 2b) are arguably a direct response to the
213 northwest-southeast SST gradient seen in Figs 1a and S2. To summarize, Africa-IO land-
214 sea contrast explains the westerlies and related subsurface nIOD pattern around its
215 peak, but anomalous zonal SST gradients also play a significant role at the early stage of
216 this nIOD.

217   To identify the main driver of the northwest-southeast SST gradient, we performed
218 slab ocean sensitivity experiments forced by the PTUBO minus CTL SW anomalies. They
219 indicate that the inhomogeneous SST cooling largely arises from the climatological cloud
220 cover distribution: the larger climatological cloud cover in the eastern equatorial IO
221 indeed acts to reduce the volcanic SW anomaly at the surface, resulting in a reduced
222 volcano-induced cooling compared to the north-western IO (Fig. S4). The resulting
223 anomalous spatial SST pattern matches qualitatively well with the climatological cloud
224 cover effect

225   We then investigate the sensitivity of the CPL response to the IO preconditioning,
226 defined as the IOD condition that would happen in autumn in the absence of the
227 Pinatubo eruption (i.e. in the CTL simulation). Such sensitivity has already been
228 discussed for ENSO (Ohba et al. 2013; Pausata et al. 2016; K17), but not for the IOD. The
229 dependence of the IO response to the Indo-Pacific initial preconditioning is assessed by
230 analysing two other pairs of 30-members ensemble experiments with and without a
231 Pinatubo-like forcing characterized respectively by El Niño and La Niña conditions in the
232 Pacific during the eruption's year (see SI; K17). We gather the three CTL 30-members
233 ensembles into a large 90-members ensemble, and then classify them depending on
234 their IOD conditions in autumn of the eruption's year, gathering members showing a
235 DMI above 0.5^{o}C (21 members), below -0.5^{o}C (49 members), and between -0.5°C and
236 0.5°C (20 members). Classifying members based on ENSO conditions in the Pacific gives
237 qualitatively similar results (with slightly less differenciation), because of the tendency

238   of ENSO and IOD events to co-occur.

239   Figure 3 displays the evolution of the DMI (Fig. 3a-c) and eastern SSH (Fig. 3d-f)

240   anomalies in CTL and PTUBO experiments for these three classes (even if the SST

241   response is different from that of an IOD, the DMI is used here to describe the SST

242   asymmetries as it broadly captures the spatial anomalies associated with this SST

243   cooling; Fig. S5 and S6). In the absence of an IOD in CTL experiment, volcanic eruptions

244   favour a nIOD-like response both at depth (∼2 cm SSH anomaly in the eastern IO; Fig.

245   3d) and at the surface (-0.4°C DMI anomaly; Fig. 3a). In the presence of a positive IOD in

246   CTL, volcanic eruptions induce a similar subsurface response (∼2cm; Fig. 3de) but a

247   larger SST response (-0.7°C; Fig. 3ab), which acts to considerably reduce the positive

248   IOD amplitude. In the presence of a negative IOD in CTL, volcanic eruptions induce a

249   weaker subsurface response (∼1.2 cm; Fig. 3f) and no significant SST gradient change

250   (Fig. 3c). The asymmetry to IO background conditions is hence larger for the SST

251   gradient than for the subsurface response. The asymmetry of the SST response mainly

252   arises from the IOD eastern pole (Fig. S5c), and could be explained by two processes

253   described below in the case of a negative IOD background condition. First, because of

254   the non-linearity of the Clausius-Clapeyron equation, the evaporation negative feedback

255   damps more the volcanically-induced relative warming in the eastern pole during a

256   negative IOD as SSTs are warmer in the eastern IO. Second, the deep background

257   thermocline in the eastern IO during a negative IOD makes the positive thermocline

258   depth anomalies forced by the eruption westerlies less efficient to warm the eastern IO

259   SST. While the asymmetry in the subsurface response is weaker, the presence of a

260   negative IOD in CTL experiment makes the subsurface response ∼1.5-2 times weaker,

261   shorter, and occuring later (only significant at the 90% level in Nov.-Dec.; not shown).

262   This suggests that the volcanically-induced SST gradient could contribute, by forcing

263   additional westerlies, to the subsurface IOD, and to its asymmetry. However, our

264   modelling setup can not precisely quantify this contribution from the ocean-atmosphere

265   coupling.

266   The robustness of the IO response to volcanic forcing derived from our single model

267   analysis is finally assessed by analysing the multi-model CMIP5 database. Composites of

268   the five historical tropical eruptions in autumn of the eruption's year in the CMIP5

269   multi-model ensemble mean (48 models/158 members, cf. SI) show patterns of surface

270   temperature, relative SST, wind stress (Fig. 4a) and sea level (Fig. 4b) that share a lot in

271 common with those obtained for our ensemble strategy using the IPSL-CM5B model for
272 the Pinatubo eruption (Fig. 1ac). This includes a larger cooling over land than over the
273 ocean, a larger SST cooling over the northwest IO, an equatorial westerly anomaly and a
274 significant subsurface oceanic response typical of a nIOD.

275   This overall consensus between our simulations and CMIP5 multi-model database
276 suggests that the results discussed in this paper are relevant for most climate models
277 used in the CMIP5 exercise. There are however significant differences between our
278 single model experiments and the CMIP5 MME multi-eruption response, generally
279 weaker (e.g. nIOD subsurface signal of only ~20% of that of a typical IOD in CMIP5 MME,
280 instead of ~30-50% in CPL). This amplitude however considerably varies among models
281 (not shown). This weaker response in the MME likely partly arises from our set-up,
282 specifically designed for the Pinatubo eruption (Fig. S1). The spread of the inter-model
283 response could also be related to the different models physics and to internal variability
284 (and random preconditioning) of each historical run.

285

286   **4) Discussion**

287

288   Analyses of dedicated coupled experiments with the IPSL-CM5B model forced by a
289 Pinatubo-like eruption and CMIP5 models historical runs demonstrate that tropical
290 volcanic eruptions force a subsurface response typical of nIOD. The surface response
291 exhibits an enhanced cooling over the northwestern IO, resulting in a
292 northwest/southeast sea surface temperature gradient. Although this inhomogeneous
293 SST pattern projects onto the classical DMI, it differs from the classical IOD SST pattern.
294 We thus term this response a « volcanic subsurface nIOD ». A hierarchy of models shows
295 that this nIOD-like subsurface signature is caused by equatorial westerly anomalies, that
296 are themselves largely an atmospheric Kelvin wave response to the fast land cooling
297 over tropical Africa. These westerlies seem to be also enhanced by the heterogeneous
298 ocean surface cooling, attributable to the heterogeneous climatological cloud cover.
299 Finally we show that the SST and subsurface responses depend on the IO
300 preconditioning, with a larger response when the system is favourable to a positive IOD
301 development, especially for the SST.
302   This volcanic subsurface nIOD is highly statistically significant but its amplitude is

303 still modest, ∼30-50% of a typical IOD in IPSL CM5B. For neutral background conditions,

304 the amplitude of the DMI SST response reaches ∼0.4°C, a value comparable to the ENSO

305 response in the same model (0.5°C Niño3.4 relative SST anomalies; K17). Given that the

306 Pinatubo eruption is relatively modest compared to other eruptions over longer

307 geological timescales, we expect the volcanic nIOD to be much stronger for very strong

308 eruptions, e.g. during the last millennium. Volcanic nIOD amplitude also considerably

309 varies among CMIP models, and will certainly depend on the model, the volcanic forcing,

310 and the eruption characteristics (strength, season, duration, latitude; Stevenson et al.

311 2016). The OCEAN process depends likely also on the volcanically-induced El Niño

312 response, which could interfere destructively with the IO local SST response by forcing

313 IO easterlies. Alleviating the dry bias in the eastern IO present in the current CMIP

314 models (e.g. Li et al. 2015) could also increase the SST gradient response by increasing

315 the climatological cloud cover effect (cf. Fig. S4), and therefore the OCEAN effect. All

316 these questions highlight the need of similar experiments in other models, as proposed

317 in the coming CMIP6 VolMIP exercise (Zanchettin et al. 2016).

318   Here we have demonstrated that a *negative* subsurface IOD develops in autumn of

319 the eruption's year. Maher et al. (2016) has interestingly briefly mentioned the tendency

320 for a *positive* IOD-like SSH pattern to develop in autumn of the eruption's *following* year

321 in CMIP models and attributed this to an indirect response to the concurrent El Niño

322 signal peaking in the Pacific. Indeed, CMIP5 MME IOD temporal evolution indicates both

323 the direct *negative* IOD response in the eruption's year and the indirect *positive* IOD the

324 following year (Fig. S6). Removing ENSO influence through linear regression confirms

325 that the positive IOD occurring the year after the eruption is mainly an indirect response

326 to the co-occurring El Niño in the Pacific, while the negative IOD response during the

327 year of the eruption is not. The direct response in CMIP MME (+0.8 cm SSH in SON of

328 eruption's year for eastern DMI pole) is of the same order of magnitude as the El Niño–

329 induced positive IOD in following year's SON (-1.2 cm; not shown).

330   The « volcanic subsurface negative IOD » does not exhibit a typical IOD signature at

331 the surface, resulting in different climate impacts. The rainfall pattern (and thus

332 atmospheric teleconnections) is indeed different (Figs S2b and S7b) from a typical IOD

333 (Fig. S3): e.g. the strong land cooling over the maritime continent favours a drying, while

334 the negative IOD-like relative SST warming (Figs 1a, S2a and S7a) favours rainfall over

335 the east IO.

336   In contrast, subsurface impacts are similar to that of a typical nIOD. Primary

337   production (PP) response in the CMIP5 models (Fig. 4c) is a mirror of SSH, notably in the

338   east IO, Bay of Bengal and Arabian Sea. This PP response fits qualitatively well with the

339   PP patterns expected from a typical IOD (e.g. Murtugudde et al. 1999, Levy et al. 2007,

340   Curie et al. 2013): a ~20% PP decrease along Sumatra (with 16 out of 18 models

341   agreeing on the sign) and a more widespread but weaker PP increase in the west IO,

342   notably along India west coast (with likely a reduction in coastal anoxia and modulation

343   of the oxygen minimum zone; Vallivattathillam et al. 2017). Concerning the IO OHC, IO

344   equatorial westerlies/negative IOD tend to discharge the tropical IO, as shown by

345   idealised switched-on westerlies LCS experiments as in Izumo et al. (2018) study (not

346   shown). El Niño also favours an IO OHC discharge via the Indonesian throughflow

347   (Sprintall and Revelard 2014; Lee et al. 2015). Hence, a tropical eruption, by favouring

348   this nIOD the eruption's year, as well as a following El Niño (Fig. S8; K17), forces a

349   significant IO OHC discharge starting in the eruption's year, the negative OHC anomaly

350   lasting then for several years in the IPSL model (not shown).

351   Understanding the sensitivity of this volcanic nIOD response to the amplitude,

352   latitude and seasonality of the eruption is the next step forward for improving post-

353   eruption climate forecasts.

354

368

369

370   Annamalai H., R. Murtugudde, J. Potemra, S. P. Xie, P. Liu, and B. Wang, 2003: Coupled dynamics in the
371   Indian Ocean: Spring initiation of the zonal mode. Deep-Sea Res. II, 50, 2305–2330.

372   Chikamoto, M. O., A. Timmermann, M. Yoshimori, F. Lehner, A. Laurian, A. Abe-Ouchi, A. Mouchet, F. Joos, C.
373   C. Raible, and K. M. Cobb (2016), Intensification of tropical Pacific biological productivity due to
374   volcanic eruptions, *Geophys. Res. Lett.*, *43*, doi:10.1002/2015GL067359.

375   Church, J. A., White, N. J., and Arblaster, J. M. (2005). Significant decadal-scale impact of volcanic eruptions
376   on sea level and ocean heat content. *Nature*, *438*(7064), 74.

377   Compo, G. P. and Sadershmukh, P. D. Oceanic influences on recent continental warming. Climate Dyn. 32,
378   333–342 (2009).

379   Currie, J. C., Lengaigne, M., Vialard, J., Kaplan, D. M., Aumont, O., Naqvi, S. W. A., and Maury, O. (2013).
380   Indian Ocean Dipole and El Nino/Southern Oscillation impacts on regional chlorophyll anomalies in
381   the Indian Ocean. *Biogeosciences*, *10*(10), 6677.

382   Dommenget, D. The ocean's role in continental climate variability and change. J. Climate 22, 4939–4952
383   (2009).

384   Gadgil, S., Vinayachandran, P. N., and Francis, P. A. (2003). Droughts of the Indian summer monsoon: Role
385   of clouds over the Indian Ocean. *Current Science*, 1713-1719.

386   Gao, C., Robock, A. and Ammann, C, 2008. Volcanic forcing of climate over the past 1500 years: An
387   improved ice core-based index for climate models. *J. Geophys. Res.* 113, D23111.

388   Gill, A. E. Some simple solutions for heat-induced tropical circulation. Q. J. R. Meteorol. Soc. 106, 447–462
389   (1980)

390   Gleckler, P. J., AchutaRao, K., Gregory, J. M., Santer, B. D., Taylor, K. E., and Wigley, T. M. L. (2006). Krakatoa
391   lives: The effect of volcanic eruptions on ocean heat content and thermal expansion. *Geophysical*
392   *Research Letters*, *33*(17).

393   Graham, N. E., and Barnett, T. P. (1987). Sea surface temperature, surface wind divergence, and convection
394   over tropical oceans. *Science*, *238*(4827), 657-659.

395   Held, I. M., and Soden, B. J. (2006). Robust responses of the hydrological cycle to global warming. *Journal of*
396   *climate*, *19*(21), 5686-5699.

397   Hourdin, F., Grandpeix, J. Y., Rio, C., Bony, S., Jam, A., Cheruy, F., ... and Dufresne, J. L. (2013). LMDZ5B: the
398   atmospheric component of the IPSL climate model with revisited parameterizations for clouds and
399   convection. *Climate Dynamics*, *40*(9-10), 2193-2222.

400   Iles, C. E. and Hegerl, G. C. The global precipitation response to volcanic eruptions in the CMIP5 models.
401   *Environ. Res. Lett.* 9, 104012 (2014).

402   Izumo T, Vialard J, Lengaigne M, de Boyer Montegut C, Behera SK, Luo J-J, Cravatte S, Masson S, Yamagata
403   T (2010a) Influence of the Indian Ocean Dipole on following year's El Nino. Nat Geosci 3:168–172

404   Izumo T, Masson S, Vialard J, de Boyer Montegut C, Behera SK, Madec G, Takahashi K, Yamagata T (2010b)
405   Low and high frequency Madden-Julian Oscillations in Austral Summer— interannual variations.
406   Clim Dyn 35:669–683

407   Izumo T, Lengaigne M, Vialard J, Luo J-J, Yamagata T, Madec G (2014) Influence of Indian Ocean Dipole and
408   Pacific recharge on following year's El Niño: interdecadal robustness. Clim Dyn 42(1–2):291–310

409   Izumo, T., Vialard, J., Dayan, H., Lengaigne, M. and Suresh, I. A simple estimation of equatorial Pacific

410   response from windstress to untangle Indian Ocean Dipole and Basin influences on El Niño. Clim.
411   Dyn. 46, 2247–2268 (2016).
412 Izumo, T., Lengaigne, M., Vialard, J., Suresh, I., and Planton, Y. (2018). On the physical interpretation of the
413   lead relation between Warm Water Volume and the El Niño Southern Oscillation. *Climate Dynamics*,
414   1-20.
415 Joshi, M. M., Gregory, J. M., Webb, M. J., Sexton, D. M., and Johns, T. C. (2008). Mechanisms for the land/sea
416   warming contrast exhibited by simulations of climate change. *Climate Dynamics*, *30*(5), 455-465.
417 Jourdain, N. C., Lengaigne, M., Vialard, J., Izumo, T., and Gupta, A. S. (2016). Further insights on the
418   influence of the Indian Ocean dipole on the following year's ENSO from observations and CMIP5
419   models. *Journal of Climate*, *29*(2), 637-658.
420 Joseph R and Zeng N. Seasonally modulated tropical drought induced by volcanic aerosol J. Clim. 24
421   2045–60 (2011)
422 Khodri, M., Izumo, T., Vialard, J., Janicot, S., Cassou, C., Lengaigne, M., ... and Robock, A. (2017). Tropical
423   explosive volcanic eruptions can trigger El Niño by cooling tropical Africa. *Nature
424   Communications*, *8*(1), 778.
425 Lee, S. K., Park, W., Baringer, M. O., Gordon, A. L., Huber, B., and Liu, Y. (2015). Pacific origin of the abrupt
426   increase in Indian Ocean heat content during the warming hiatus. *Nature Geoscience*, *8*(6), 445.
427 Lehner, F., A. P. Schurer, G. C. Hegerl, C. Deser, and T. L. Frölicher (2016), The importance of ENSO phase
428   during volcanic eruptions for detection and attribution, Geophys. Res. Lett., 43,
429   doi:10.1002/2016GL067935.
430 Lévy, M., Shankar, D., André, J. M., Shenoi, S. S. C., Durand, F., and de Boyer Montégut, C. (2007). Basin-wide
431   seasonal evolution of the Indian Ocean's phytoplankton blooms. *Journal of Geophysical Research:
432   Oceans*, *112*(C12).
433 Li, G., Xie, S. P., and Du, Y. (2015). Monsoon-induced biases of climate models over the tropical Indian
434   Ocean. *Journal of Climate*, *28*(8), 3058-3072.
435 Madec, G. (2015). NEMO ocean engine. *IPSL edition.*
436 Maher, N., S. McGregor, M. H. England, and A. Sen Gupta. Effects of volcanism on tropical variability,
437   Geophys. Res. Lett., 42, 6024–6033, doi:10.1002/2015GL064751 (2015).
438 Matsuno, T., 1966: Quasi-geostrophic motions in the equatorial area. *J. Meteor. Soc. Japan,* 44, 25–43.
439 McCormick et al. 1995, Atmospheric effects of Mount Pinatubo, Nature
440 McCreary, J. P. Modelling wind-driven ocean circulation. JIMAR 80-0029, HIG 80-3, Univ. of Hawaii,
441   Honolulu, pp. 64 (1980).
442 McGregor, S. and Timmermann, A. The effect of explosive tropical volcanism on ENSO. J. Climate 24, 2178–
443   2191 (2011).
444 Mignot, J., Khodri, M., Frankignoul, C., and Servonnat, J. (2011). Volcanic impact on the Atlantic Ocean over
445   the last millennium. *Climate of the Past Discussions*, *7*, 2511-2554.
446 Murtugudde, R. G., Signorini, S. R., Christian, J. R., Busalacchi, A. J., McClain, C. R., and Picaut, J. (1999).
447   Ocean color variability of the tropical Indo-Pacific basin observed by SeaWiFS during 1997–
448   1998. *Journal of Geophysical Research: Oceans*, *104*(C8), 18351-18366.
449 Murtugudde R, McCreary JP, Busalacchi AJ (2000) Oceanic processes associated with anomalous events in

450   the Indian Ocean with relevance to 1997–1998. J Geophys Res 105:3295–3306

451 Ohba M., H. Shiogama, T. Yokohata, and M. Watanabe. Impact of strong tropical volcanic eruptions on
452   ENSO simulated in a coupled GCM. *J. Climate*, 26, 5169–5182 (2013).

453 Pausata F.S.R., Christina Karamperidou, Rodrigo Caballero, David S. Battisti. (2016) ENSO response to
454   high-latitude volcanic eruptions in the Northern Hemisphere: The role of the initial conditions.
455   *Geophysical Research Letters*.

456 Rebert, J. P., Donguy, J. R., Eldin, G., and Wyrtki, K. (1985). Relations between sea level, thermocline depth,
457   heat content, and dynamic height in the tropical Pacific Ocean. *Journal of Geophysical Research:*
458   *Oceans*, *90*(C6), 11719-11725.

459 Reverdin G, Cadet D, Gutzler D (1986) Interannual displacements of convection and surface circulation
460   over the equatorial Indian Ocean. Q J R Meteorol Soc 112:43–46

461 Reynolds M.W. 1993 Impact of Mount Pinatubo aerosols on satellite-derived SSTs, J.Clim. 6.

462 Robock, A. Volcanic eruptions and climate. Rev. Geophys. 38, 191–219 (2000).

463 Saji NH, Goswami BN, Vinayachandran PN, Yamagata T (1999) A dipole mode in the tropical Indian Ocean.
464   Nature 401:360–363.

465 Saji, N. H., Xie, S. P., and Yamagata, T. (2006). Tropical Indian Ocean variability in the IPCC twentieth-
466   century climate simulations. *Journal of Climate*, *19*(17), 4397-4417

467 Samson G., S. Masson, F. Durand, P. Terray, S. Berthet and S. Jullien, 2016. Roles of land surface albedo and
468   horizontal resolution on the Indian summer monsoon biases in a coupled ocean–atmosphere
469   tropical-channel model. Clim Dyn., DOI 10.1007/s00382-016-3161-0

470 Schneider, D. P., C. M. Ammann, B. L. Otto-Bliesner, and D. S. Kaufman (2009), Climate response to large,
471   high-latitude and low-latitude volcanic eruptions in the Community Climate System Model, J.
472   Geophys. Res., 114, D15101, doi:10.1029/2008JD011222.

473 Schott, F. A., Xie, S. P., and McCreary, J. P. (2009). Indian Ocean circulation and climate variability. *Reviews*
474   *of Geophysics*, *47*(1).

475 Sprintall, J., and Révelard, A. (2014). The Indonesian Throughflow response to Indo-Pacific climate
476   variability. *Journal of Geophysical Research: Oceans*, *119*(2), 1161-1175.

477 Sobel, A. H., Nilsson, J., and Polvani, L. M. (2001). The weak temperature gradient approximation and
478   balanced tropical moisture waves. *Journal of the atmospheric sciences*, *58*(23), 3650-3665.

479 Soden, B. J., Wetherald, R. T., Stenchikov, G. L. and Robock, A. Global cooling after the eruption of mount
480   pinatubo: a test of climate feedback by water vapor. Science 296, 727–730 (2002).

481 Stenchikov, G., Delworth, T. L., Ramaswamy, V., Stouffer, R. J., Wittenberg, A., and Zeng, F. (2009). Volcanic
482   signals in oceans. *Journal of Geophysical Research: Atmospheres*, *114*(D16).

483 Stevenson S., B. Otto-Bliesner, J. Fasullo, and E. Brady. ''El Niño Like'' Hydroclimate Responses to Last
484   Millennium Volcanic Eruptions. J. Clim., DOI: 10.1175/JCLI-D-15-0239.1 (2016).

485 Suresh, I., Vialard, J., Lengaigne, M., Han, W., McCreary, J., Durand, F., and Muraleedharan, P. M. (2013).
486   Origins of wind-driven intraseasonal sea level variations in the North Indian Ocean coastal
487   waveguide. *Geophysical Research Letters*, *40*(21), 5740-5744.

488   Suresh, I., Vialard, J., Izumo, T., Lengaigne, M., Han, W., McCreary, J., and Muraleedharan, P. M. (2016).
489   Dominant role of winds near Sri Lanka in driving seasonal sea level variations along the west coast of
490   India. *Geophysical Research Letters*, *43*(13), 7028-7035.

491   Taylor K. E., R. J. Stouffer, and G. A. Meehl, 2012. An Overview of CMIP5 and the Experiment Design. Bull.
492   Amer. Meteor. Soc., 93, 485–498

493   Vallivattathillam, P., Iyyappan, S., Lengaigne, M., Ethé, C., Vialard, J., Levy, M., ... and Naqvi, W. (2017).
494   Positive Indian Ocean Dipole events prevent anoxia off the west coast of India. *Biogeosciences*, *14*(6),
495   1541

496   Vecchi, G. A., and Soden, B. J. (2007). Global warming and the weakening of the tropical circulation. *Journal
497   of Climate*, *20*(17), 4316-4340.

498   Webster PJ, Moore A, Loschnigg J, Leban M (1999) Coupled dynamics in the Indian Ocean during 1997–
499   1998. Nature 401:356–360

500   Xie, S.-P., H. Annamalai, F. Schott, and J. P. McCreary Jr., 2002: Origin and predictability of south Indian
501   Ocean climate variability. *J. Climate,* **15,** 864–874.

502   Yamagata, T., S. K. Behera, J.-J. Luo, S. Masson, M. R. Jury, and S. A. Rao, 2004: Coupled ocean–atmosphere
503   variability in the tropical Indian Ocean. *Earth's Climate: The Ocean– Atmosphere Interaction, Geophys.
504   Monogr.,* Vol. 147, Amer. Geophys. Union, 189–212.

505   Zanchettin D., M. Khodri, C. Timmreck, M. Toohey, A. Schmidt, E. P. Gerber, G. Hegerl, A. Robock, F. S.
506   Pausata, W. T. Ball, S. E. Bauer, S. Bekki, S. S. Dhomse, A. N. LeGrande, G. W. Mann, L. Marshall, M.
507   Mills, M. Marchand, U. Niemeier, V. Paulain, A. Rubino, A. Stenke, K. Tsigaridis, and F. Tummon (2016)
508   The Model Intercomparison Project on the climatic response to Volcanic forcing (VolMIP):
509   Experimental design and forcing input data. GeoScientific Model Development discussion paper, MS
510   No.: gmd-2016-68. Special Issue: Coupled Model Intercomparison Project Phase 6 (CMIP6)
511   Experimental Design and Organization.

512

Figures captions

Figure 1. Indian Ocean response in the autumn following a Pinatubo-like eruption. (a) 2m air temperature (T2m, in ºC, shading) and surface wind stress (N m^{-2}, vectors) difference between PTUBO and CTL ensemble coupled experiments (CPL) in autumn (September-November), a few months after the eruption in June. (b) as in (a), but for the ALL AGCM (°C). (c) as (a), but for the SSH (cm) response. (d) SSH response in an LCS model experiment forced by PTUBO-CTL wind stress anomalies (cm). 90% significance level in black contours (dashed when negative values), except in (a) in which red/green contours show positive/negative relative SST (ºC). Windstress overlaid in black when 90% significant, grey otherwise.

Figure 2. Main mechanisms driving the IO response. Equatorial IO zonal wind stress (upper row, N.m^{-2}) and eastern equatorial IO SSH response in the LCS (middle row, cm) for **(left)** CPL (black) and ALL (purple) experiments and for **(right)** LAND (cyan), LAND_Africa (green), OCEAN (dark blue) and ATM (red) sensitivity experiments. Circles indicate when anomalies are significant at the 90% level. Light color shading indicate the 90% confidence interval for selected experiments. Zonal wind stress is averaged over [60°E-90°E ; 2.5°N-2.5°S] region and SSH over the [90°-110°E ; 0°-10°S] region.

Fig. 3. Influence of background IO conditions on the IPSL CM5B response to the eruption. (a) SST DMI anomaly (with regards to historical run climatology, in ^{o}C) for the control ensemble members (black) and the Pinatubo simulations (purple) for members showing neutral IOD conditions in SON 1991 in the control simulations (49 members). (b) Same for positive IOD conditions (21 members). (c) Same for negative IOD conditions (20 members). d, e, f: same for DMI east pole SSH. 90% intervals of confidence in light shading.
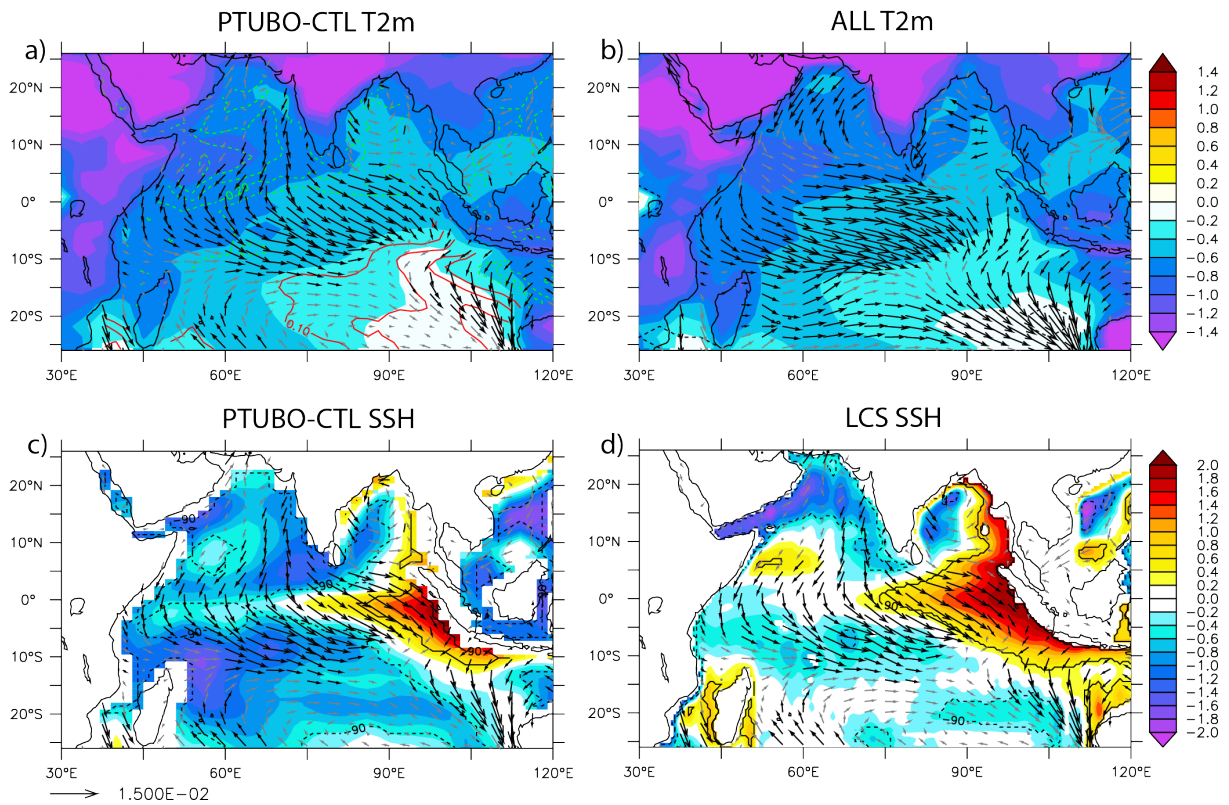
Fig. 4. IO response in the autumn following tropical volcanic eruptions in CMIP models. CMIP response to the last five large tropical eruptions in SON of eruption's year for (a) 2m air temperature (^{o}C, positive/negative relative SST in red/green contours), (b) SSH (cm) and (c) Primary production (PP, unit : 10^{-8} mol m^{-2} s^{-1}). Wind stress are overlaid in black when 90% significant, grey otherwise. 90% significance level in black contours (dashed when negative values), except for PP, whis is available for less models,
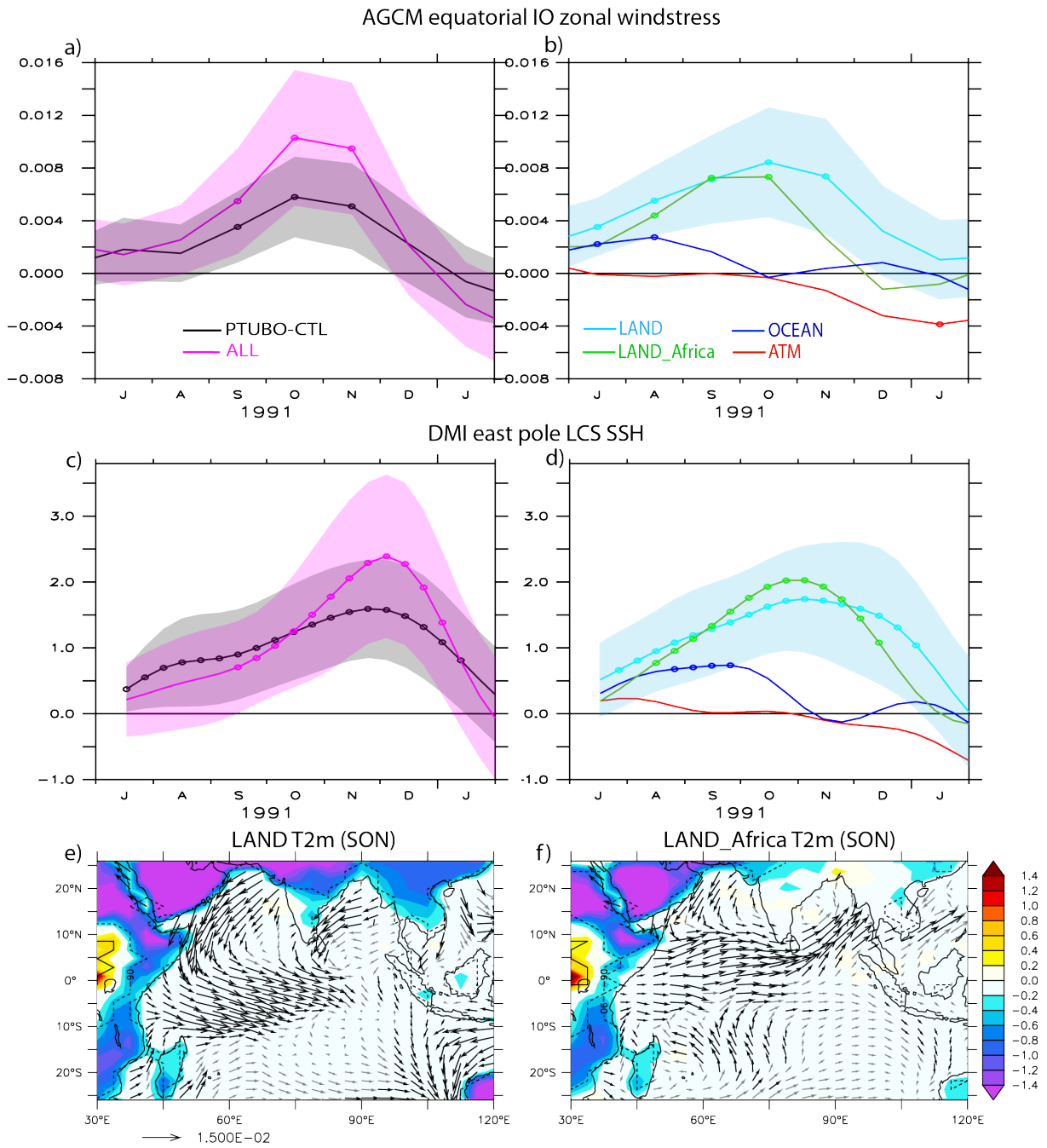
546   for which significancy is defined when there are two times more models of the adequate

547   sign by solid color shading (white-stripped when not significant).
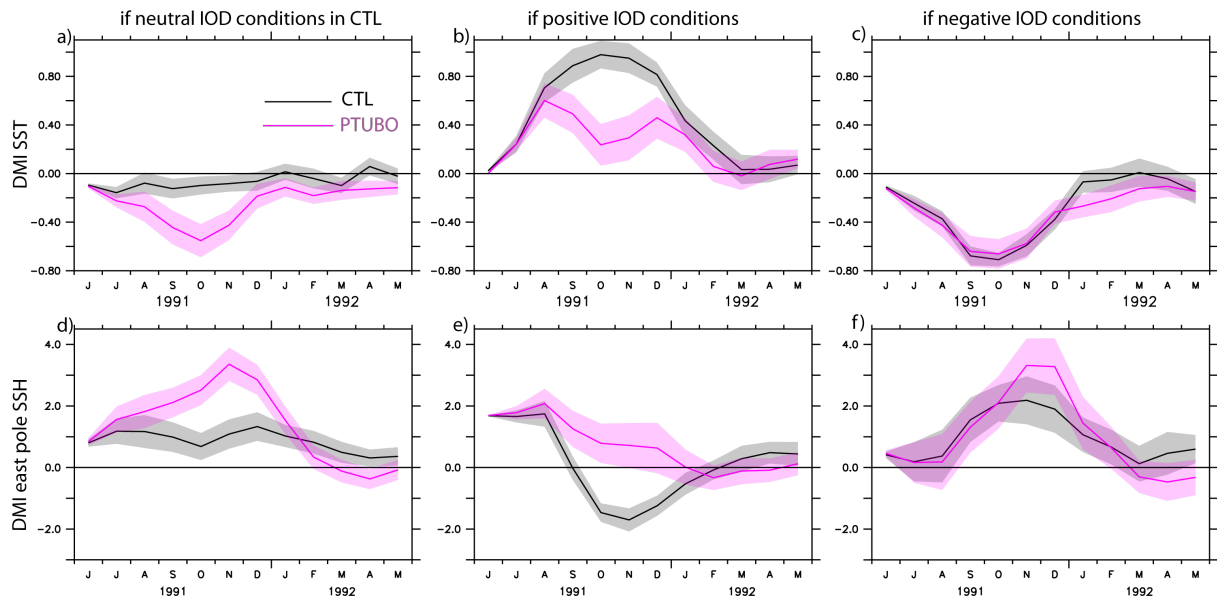
Figures 1 to 4 with captions.

Figure 1. Indian Ocean response in the autumn following a Pinatubo-like eruption. (a) 2m air temperature (T2m, in ºC, shading) and surface wind stress (N m^{-2}, vectors) difference between PTUBO and CTL ensemble coupled experiments (CPL) in autumn (September-November), a few months after the eruption in June. (b) as in (a), but for the ALL AGCM (°C). (c) as (a), but for the SSH (cm) response. (d) SSH response in an LCS model experiment forced by PTUBO-CTL wind stress anomalies (cm). 90% significance level in black contours (dashed when negative values), except in (a) in which red/green contours show positive/negative relative SST (ºC). Windstress overlaid in black when 90% significant, grey otherwise.
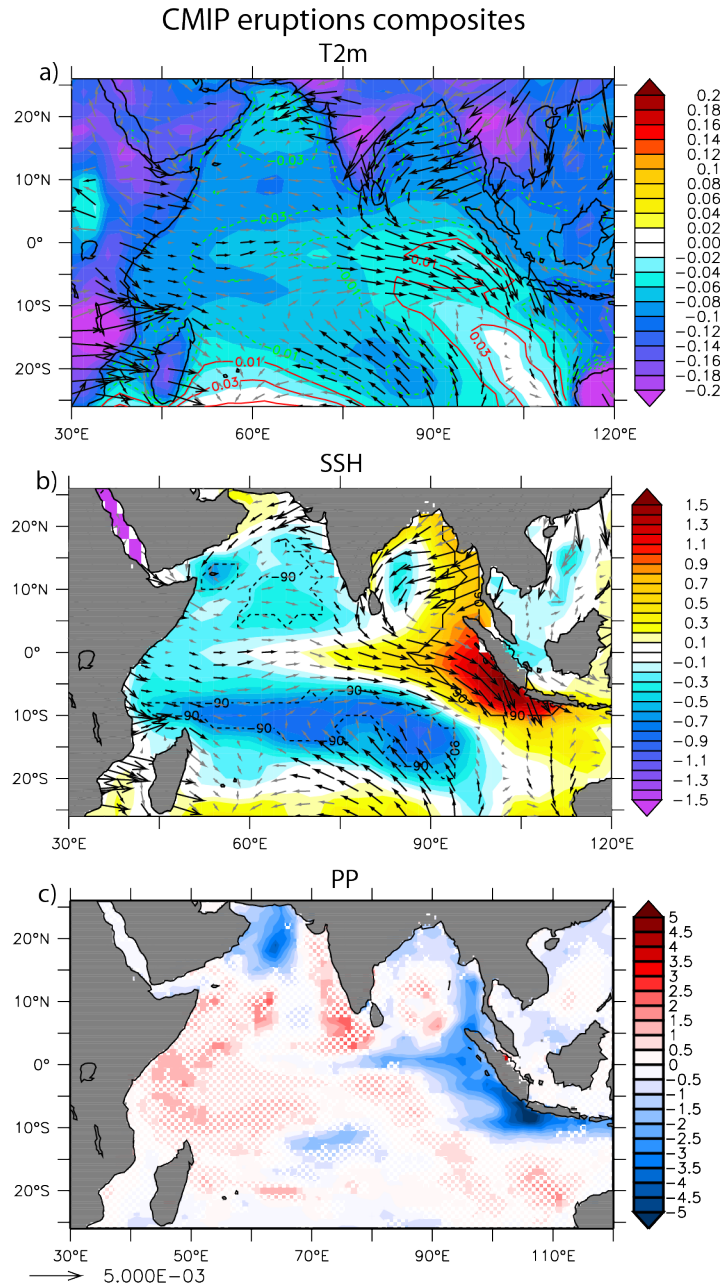
Figure 2. Main mechanisms driving the IO response. Equatorial IO zonal wind stress (upper row, N.m^{-2}) and eastern equatorial IO SSH response in the LCS (middle row, cm) for **(left)** CPL (black) and ALL (purple) experiments and for **(right)** LAND (cyan), LAND_Africa (green), OCEAN (dark blue) and ATM (red) sensitivity experiments. Circles indicate when anomalies are significant at the 90% level. Light color shading indicate the 90% confidence interval for selected experiments. Zonal wind stress is averaged over [60°E-90°E ; 2.5°N-2.5°S] region and SSH over the [90°-110°E ; 0°-10°S] region.

Fig. 3. Influence of background IO conditions on the IPSL CM5B response to the eruption. (a) SST DMI anomaly (with regards to historical run climatology, in ºC) for the control ensemble members (black) and the Pinatubo simulations (purple) for members showing neutral IOD conditions in SON 1991 in the control simulations (49 members). (b) Same for positive IOD conditions (21 members). (c) Same for negative IOD conditions (20 members). d, e, f: same for DMI east pole SSH. 90% intervals of confidence in light shading.

CMIP eruptions composites

28

29 **Fig. 4. IO response in the autumn following tropical volcanic eruptions in CMIP**
30 **models.** CMIP response to the last five large tropical eruptions in SON of eruption's year
31 for (a) 2m air temperature (°C, positive/negative relative SST in red/green contours),
32 (b) SSH (cm) and (c) Primary production (PP, unit : 10^{-8} mol m^{-2} s^{-1}). Wind stress are
33 overlaid in black when 90% significant, grey otherwise. 90% significance level in black
34 contours (dashed when negative values), except for PP, whis is available for less models,
35 for which significancy is defined when there are two times more models of the adequate
36 sign by solid color shading (white-stripped when not significant).

Supplementary Information for "A subsurface Indian Ocean Dipole response to tropical volcanic eruptions"

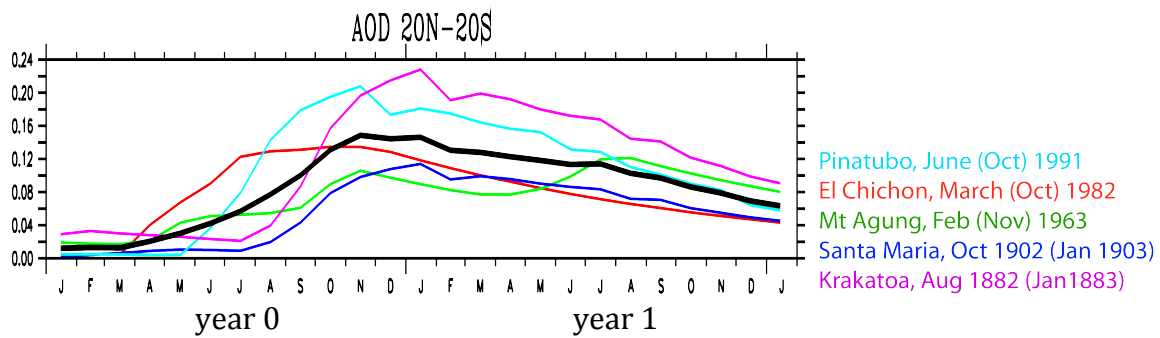Takeshi Izumo, Myriam Khodri, Matthieu Lengaigne, Iyyappan Suresh

Figure S1. Tropical average (20°N-20°S) of Stratospheric Aerosol Optical Depth (AOD ; Gao et al. 2008) for the last 5 tropical stratospheric eruptions from the historical period, from year 0 (year of the eruption) to year 1 (eruption's following year). The starting (peaking) month and year for each eruption is indicated on the right-hand side. The black line indicates the mean of the 5 eruptions. This figure illustrates the large diversity in tropical AOD amplitude, seasonality and temporal evolution, and the fact that the Pinatubo eruption had the largest radiative forcing in summer-fall, the season that matters for the development of the subsurface IOD studied here.
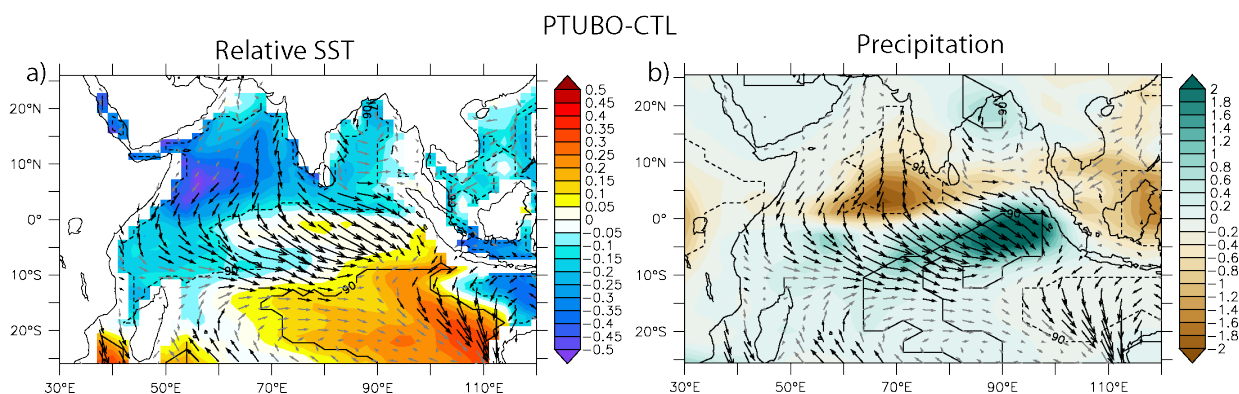

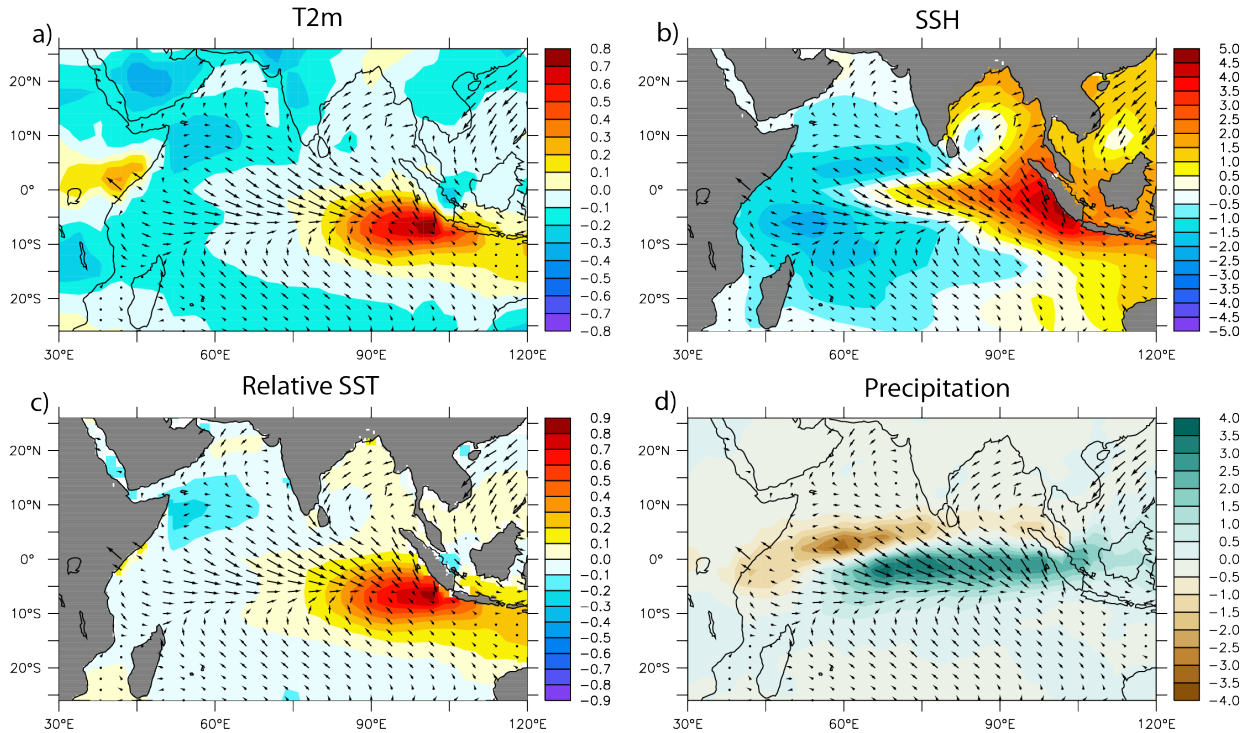**Figure S2.** As Fig. 1a (difference PTUBO-CTL), but for (a) relative SST (°C) and (b) precipitation (mm/day).

Figure S3. Typical IOD pattern in IPSL-CM5B-LR. Regression of (a) 2m air temperature (°C), (b) SSH (cm), (c) relative SST (°C) and (d) precipitation (mm/day) onto normalised DMI in SON (its standard deviation being 0.55°C), in IPSL-CM5B-LR CMIP5 historical run.
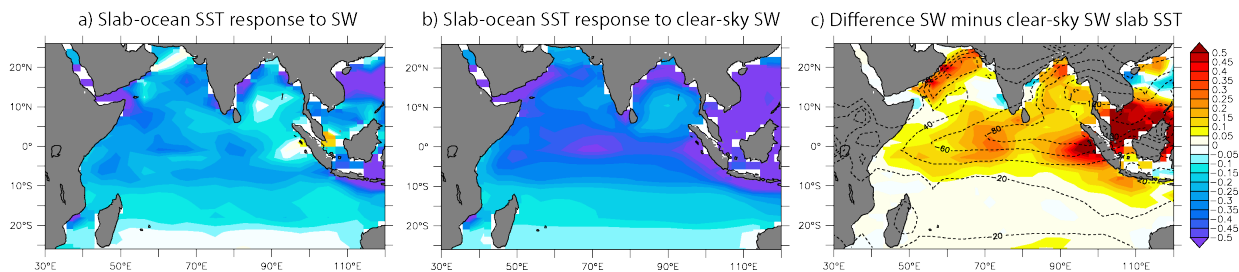

Figure S4. Slab ocean response to PTUBO-CTL SW forcing in July-September (JAS, when OCEAN has a significant effect on equatorial zonal wind stress; cf. Fig. 2)**.** (a) Slab-ocean SST response to PTUBO-CTL SW forcing (°C). (b) Slab-ocean SST response to clear-sky PTUBO-CTL SW forcing. (c) Difference between the two, SW minus clear-sky SW, i.e. mainly the effect of climatological cloud cover shown in contours (effect inferred from IPSL-CM5B-LR climatological SW minus climatological clear-sky SW; W.m^{-2}). See details about this slab ocean using a spatially-varying MLD climatology in supplementary section 3. Note that, while the cooling and its heterogeneity is mainly due to the SW anomalies, there is a notable additional effect of latent heat flux – through windspeed anomalies – that could explain the relative SST warming seen south of 10°S in the southeast Indian Ocean, west of Australia, in Fig. S2a and Fig. 1a. The northwest anomalies there (possibly related to the anticyclonic anomalies created by the strong land cooling of Australia; not shown) oppose the trade winds, thereby decreasing local windspeed and evaporation. A similar windspeed effect, but of opposite sign, seems to have also played a role in re-inforcing the Arabian Sea cooling (southwesterly anomalies reinforcing the monsoon low-level jet in JAS; not shown).
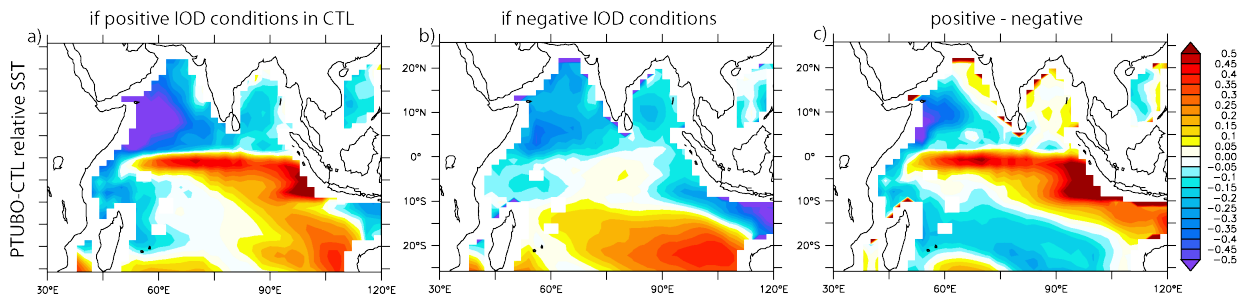
Figure S5. Influence of background IO conditions on the IPSL CM5B relative SST response. (a) As Fig. S2a, but for members showing positive IOD conditions in SON 1991 in the control simulations. (b) same for negative IOD conditions. (c) difference between panels b and a. This figure highlights the asymmetries in the SST response, with a much larger negative Northwest-Southeast SST gradient in the background positive IOD case, which projects onto the DMI poles (cf. Fig. 3a,b,c).
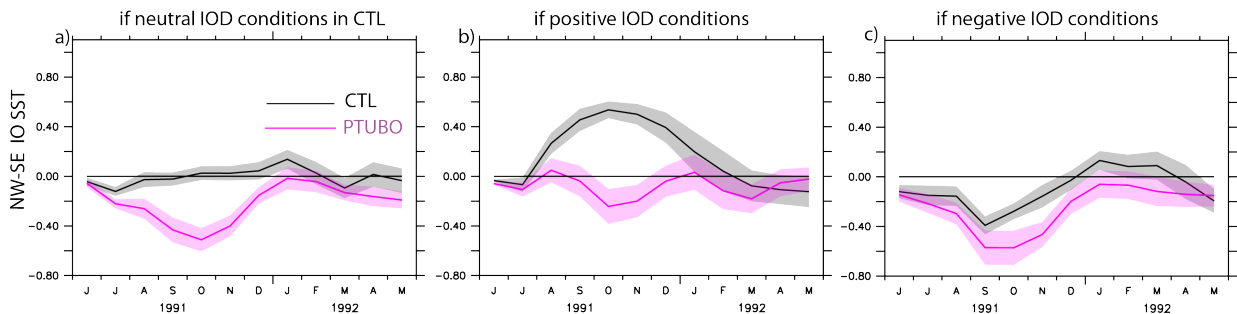
Figure S6. Influence of background IO conditions on the IPSL CM5B NW-SE SST gradient response. (a) As Fig. 3abc, but for an index especially developped to capture the Northwest – Southeast (NW-SE) SST gradient forced by the eruption, defined as the SST difference between the 50-70ºE, 20ºN-0ºN and 90-110ºE, 0-20ºS regions. The PTUBO-CTL difference is even larger than for the DMI shown in Fig. 3abc, and is still significant in the negative IOD background case.
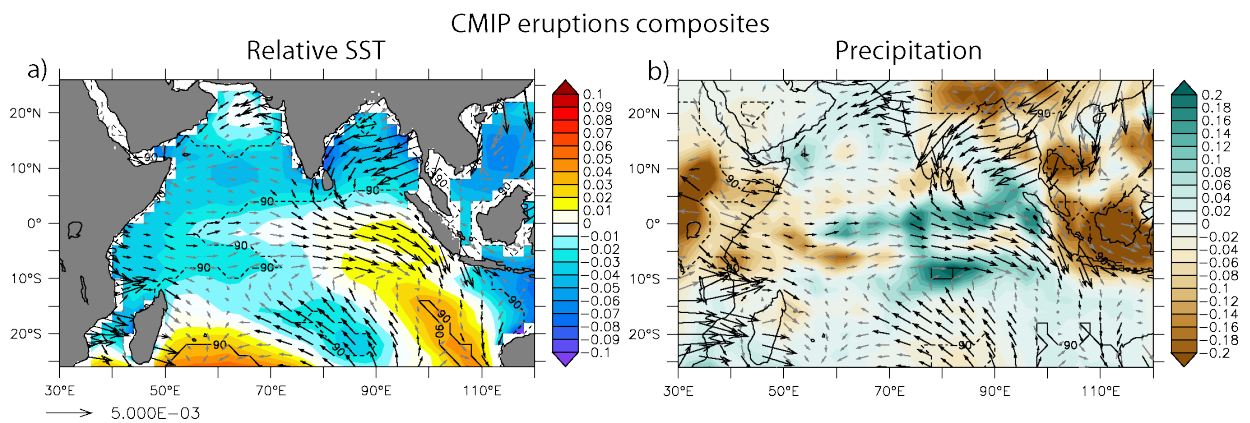
Figure S7. As Fig. 4 (CMIP eruptions composites), but for (a) relative SST (^{o}C) and (b) precipitation (mm/day).
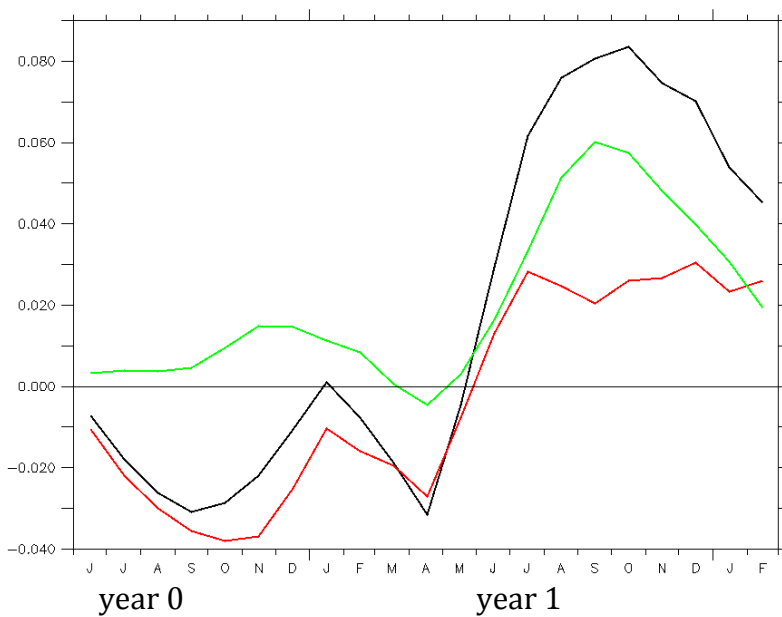

Fig. S8: DMI temporal evolution from year 0 to year 1 in CMIP MME (black), external influence of ENSO on the DMI (green ; inferred from the linear regression of DMI on Nino3.4 SST computed for each CMIP model separately), and the DMI response independent of simultaneous ENSO conditions (red = black – green).

1. Inhomogeneous cooling, relative SST and rainfall responses to eruptions

To understand the rainfall response, as the eruption induces an overall cooling, especially in the tropics, it is relevant to use the relative SST, simply defined as the SST minus its tropical mean (20°N-20°S), a concept initially developped for global warming (Held and Soden 2006, Vecchi and Soden 2007), but which is also relevant here, as the volcanic aerosol optical depth radiative forcing is rather homogeneous zonally along the tropical band and evolves relatively slowly with regards to tropospheric tropical adjustment time (see also K17, which shows the relevance of using relative SST to understand the El Niño response to tropical eruptions).

Concerning the physical process behind the faster land cooling than ocean one, it is likely related to the larger lapse rate over the land, as the troposphere over the land generally is drier than that over the oceans (as suggested by global warming studies, e.g. Joshi et al., 2008), rather than to the lower heat capacity of the land (as suggested by some earlier studies for volcanism). The upper tropospheric cooling is relatively uniform in the tropics: a larger lapse rate hence yields a larger surface cooling over land, in particular in dry areas (same suggested mechanism, for a cooling instead of a warming, as in the case of global warming discussed in e.g. Sobel et al., 2001; Joshi et al. 2008).

2 The IPSL-CM5B-LR model and the AGCM experimental strategy (detailed description)

In the present study, we use the same set of simulations as in K17 including experiments with the Institut Pierre Simon Laplace (IPSL) CM5B-LR coupled climate model, atmospheric and oceanic sensitivity ensemble experiments, with and without a Pinatubo-like forcing, to identify the main mechanisms at play. We choose the Pinatubo eruption (June 15th, 1991), as it is the largest and best-documented tropical stratospheric eruption of the instrumental period. The details of these experiments are already described in K17 and we only summarize here their salient features. The atmospheric component is LMDZ5B (Hourdin et al. 2013) with 39 pressure levels (including 18 in the stratosphere) and a horizontal resolution of 1.87° in latitude and 3.75° in longitude. It uses ORCHIDEE as its land surface component. It is coupled to the NEMO3.2 oceanic component (Madec 2015) (31 vertical levels, and an horizontal resolution of about 2°, with a refinement of the latitudinal resolution to 0.5° near the equator; ORCA2 grid). This model is able to capture reasonably well the main observed IOD features (Jourdain et al. 2016).

The above IPSL-CM5B-LR climate model is forced by Pinatubo stratospheric aerosol optical depth (AOD) data provided by Gao et al. (2008). The 30-member ensemble experiment is run from 1st of June of a selected year from the historical run, chosen to be close to 1990s greenhouses gases and tropospheric aerosols concentrations, to lie more than 5 years away from any volcanic eruption and to lead to neutral El Nino Southern Oscillation (ENSO) conditions in the absence of volcanic forcing, avoiding any interference with external ENSO forcing (K17). For this initial state, 30 members were generated by adding a small white noise on the initial SST. For Fig. 3, we used two others 30-member ensemble experiments starting from the 1st June of two other selected years, these two years being characterized respectively by El Niño and La Niña conditions in the Pacific.

Corresponding control ensembles starting from the same initial conditions but without Pinatubo volcanic forcing were analysed (i.e. 3 CTL ensembles of 30 members each).

K17 have developed targeted ensemble experiments using the atmospheric component of the IPSL-CM5B model forced by the outputs of the coupled model ensemble (see K17 for details) to investigate the respective role of the following three processes in the generation of atmospheric anomalies, notably windstress :

(1) the direct effect of volcanic radiative forcing on clouds and atmospheric vapour content (Soden et al. 2002), potentially altering the atmospheric vertical structure and inducing an atmospheric dynamical response (referred to as ATM). Volcanic aerosol forcing is included in ATM, but the surface albedo is modified so that continental surfaces do not cool in response to volcanic forcing in this experiment.

(2) the indirect effects of volcanic forcing through the SST cooling and its spatial heterogeneities, and related horizontal SST gradients (OCEAN; inferred from the difference between the AGCM forced by the SST from PTUBO experiment and the unperturbed AGCM experiment, cf. K17). The OCEAN experiment includes not only the effect of SST anomalies that develop in response to volcanic forcing, i.e. the initial thermodynamical forcing and the slab ocean response, but also the positive Bjerkness feedback (i.e. the LCS dynamical response) once nIOD-like relative SST anomalies have started developing. However, the dominance of the LAND process (cf. Fig. 2) suggests that coupling processes, notably the Bjerknes feedback, should only be of secondary importance during the summer-fall of the eruption year, at least in our experimental framework.

(3) continents cool faster than the ocean in response to volcanic forcing. The third and last experiment (referred to as LAND) tests the effect of this differential surface cooling between land and ocean. In LAND, there is no prescribed aerosol forcing as in OCEAN, but the land surface albedo modification enforces a land surface cooling that is consistent with that of the IPSL-CM5B coupled model experiment.

This strategy allows land surface temperature variations in OCEAN experiments, in response to SST anomalies, as described in the context of global warming (Compo and Sadershmukh 2009, Dommenget 2009). It is hence more physically consistent than experiments that directly constrain land surface temperature (Ohba et al. 2013), which can result in an exaggerated land cooling and land–ocean gradients. An additionnal sensitivity experiment from K17, of interest here, explores the effect of the faster land cooling only over one specific region, Africa (LAND-Africa). An additional experiment (ALL) that includes all three LAND, OCEAN and ATM processes reproduces reasonably well the anomalies simulated by the IPSL-CM5B ensemble simulation (Fig. 1a,b and Fig. 2a,c), confirming the relevance of this two-tier approach for understanding how volcanic eruptions induce equatorial IO westerlies.

3 Linear Continuously Stratified (LCS) model and slab ocean model

The equatorial Indian Ocean dynamical oceanic response to wind-stress anomalies resulting from each process is estimated separately by forcing a linear continuously stratified (LCS; McCreary, 1980) ocean model of the Indo-Pacific region (same configuration as in Izumo et al. 2016, 2018). This LCS model, that resolves vertical baroclinic modes (with mainly the first two modes contributing; not shown), realistically simulates SSH anomalies (see Suresh et al. 2013, 2016 ; Izumo et al. 2016, 2018; K17 for further details).

A simple slab ocean mixed layer equation is also used, to simulate the SST thermodynamical response to the eruption-induced ShortWave (SW) flux anomalies (see Supplementary Information), following the approach of McGregor and Timmerman (2011). This simple slab ocean mixed layer equation is based on the following linear SST equation to realistically resolve the variations of SST forced by Pinatubo shortwave anomalies (SW'):

$$\frac{dSST\prime}{dt} = SW\prime/(\rho C_p MLD) - \alpha SST\prime$$

the "prime" denoting the Pinatubo-forced anomalies (i.e. Pinatubo-forced IPSL PTUBO run minus control IPSL CTL run). SW is here the SW surface net downward flux minus the downward SW at the bottom of the mixed layer. Mixed Layer Depth (MLD) is the local MLD monthly climatology, inferred from the depth at which the potential density is $0.06 kg/m^3$ larger than at 10m depth (equivalent to a 0.2ºC decrease in temperature) of the CTL IPSL run. The forcing is simply from this SW', other heat fluxes being parameterised as a constant Newtonian damping $-\alpha$ SST', with the typical damping timescale $1/\alpha$ = 2 months, as in Izumo et al. (2016). The time integration (with initial start in June 1991) of the above linearized SST tendency equation gives us the *SST'* temporal evolution. A reference simulation is set up using the MLD climatology and the SW' anomalies induced by Pinatubo in IPSL ensemble mean. In addition to the clear-sky sensitivity experiment (in which the clear-sky SW forcing is rather zonally-homogeneous in the tropical band) shown in Figure S4, we used this very simple model to evaluate the roles of the zonal variations of SW' (mainly related to climatological cloud cover/albedo spatial variations) and of mean MLD zonal variations on the SST response to Pinatubo, and so on SST zonal gradient. While the former explains most of the actual gradient, the latter does not: the zonal variations of the MLD climatology have less impact on equatorial SST gradient (not shown) and generally oppose those from climatological cloud cover distribution (MLD, being shallower in the east, will tend to increase cooling there).

4 CMIP5 simulations

To assess the robustness of our results with our single model experiments, we also analyse historical simulations from the Climate Model Intercomparison Project phase 5 (CMIP5) dataset (Taylor et al. 2012) over the 1861-2005 period (see Suppl. Table S1). To estimate their responses to tropical volcanism, we composited the 5 largest tropical eruptions (cf. K17 for details). 49 models were available for 2m and surface temperature, 44 for windstress, 37 for SSH and 18 for Primary Productivity. We used all models available for each field. The Multi-Model-Ensemble (MME) mean is computed by first

averaging all members for each model to smooth out internal noise before averaging between models. We checked that the results are qualitatively insensitive to the choice of these methods: using the first member of each model, or reducing the number of models, gives similar results, but with slightly more internal noise.

In preprocessing, we removed the 10 previous years sliding climatology in CMIP historical runs, to filter out possible trends and interdecadal variability. 3 months running mean (for maps) or Hanning filter (for time series) is applied on data to reduce the strong intraseasonal variability of the tropics. In order to better compare models, which possibly have different typical interannual variations, we also computed « standardised » amplitudes of some relevant indices, by normalizing by the interannual standard deviation computed for Sept.-Nov. (SON) over the full historical run period and for each model.

In addition to the main analyses shown in the present paper, we have also done a CMIP inter-eruption comparison. We have compared various eruptions in CMIP in terms of impacts on the IO. At least all the eruptions had a subsurface negative IOD in SON0, except for Krakatau with neutral IOD in autum of yr0 (eruption in August, possibly too late to trigger a negative IOD; not shown), even if there is a large inter-model diversity because of the sensitivity to initial conditions (and so to internal variability of each model/member) that lowers the signal to noise ratio.

Table S1. List of the 48 CMIP models (158 members) used in this study, and the maximum number of members in each model (mainly for surface air temperature at 2m and sea level height).

Institute name	Model name	Max. number of members
BCC	bcc-csm1-1	3
	bcc-csm1-1-m	3
BNU	BNU-ESM	1
CCCma	CanESM2	5
CMCC	CMCC-CESM	1
	CMCC-CM	1
	CMCC-CMS	1
CNRM-CERFACS	CNRM-CM5	10
	CNRM-CM5-2	1
CSIRO-BOM	ACCESS1-0	1
	ACCESS1-3	3
CSIRO-QCCCE	CSIRO-Mk3-6-0	10
FIO	FIO-ESM	3
ICHEC	EC-EARTH	9
INM	inmcm4	1
IPSL	IPSL-CM5A-LR	6
	IPSL-CM5A-MR	3
	IPSL-CM5B-LR	1
LASG-CESS	FGOALS-g2	1
LASG-IAP	FGOALS-s2	1
MIROC	MIROC5	5
	MIROC-ESM	3
	MIROC-ESM-CHEM	1
MOHC	HadCM3	10
	HadGEM2-CC	3
	HadGEM2-ES	4
MPI-M	MPI-ESM-LR	3
	MPI-ESM-MR	3
	MPI-ESM-P	2
MRI	MRI-CGCM3	3
	MRI-ESM1	3
NASA-GISS	GISS-E2-H	6
	GISS-E2-H-CC	1
	GISS-E2-R	6
	GISS-E2-R-CC	1
NCAR	CCSM4	6
NCC	NorESM1-M	3
	NorESM1-ME	1
NIMR-KMA	HadGEM2-AO	1
NOAA-GFDL	GFDL-CM2p1	10
	GFDL-CM3	5
	GFDL-ESM2G	1
	GFDL-ESM2M	1
NSF-DOE-NCAR	CESM1-BGC	1
	CESM1-CAM5	3
	CESM1-FASTCHEM	3
	CESM1-WACCM	4
Total number of models/members	48	158